

# Broad Wavelength Range Metal-Enhanced Fluorescence Using Nickel Nanodeposits

Yongxia Zhang, Anatoliy Dragan, and Chris D. Geddes\*

*Institute of Fluorescence, Laboratory for Advanced Medical Plasmonics, and Laboratory for Advanced Fluorescence Spectroscopy, University of Maryland Biotechnology Institute, 701 East Pratt Street, Baltimore, Maryland 21202*

Received: February 2, 2009; Revised Manuscript Received: June 15, 2009

We describe the use of surface-deposited nickel nanoparticles to enhance the fluorescence signatures of fluorophores. Different density Ni nanoparticulate substrates were fabricated and characterized using both AFM and optical absorption techniques. When fluorophores were placed in close proximity to the substrates, metal-enhanced fluorescence (MEF) was observed. The wavelength dependence of the metal-enhanced fluorescence corresponded with numerical finite-difference time-domain simulations also showing a broad range (500–800 nm) for the enhanced electric field of Ni nanoparticles as compared with traditionally  $\approx 400$  to 500 nm for the widely used Ag nanoparticles. This broad wavelength range for an enhanced electric field enables nickel nanoparticles to enhance near-field dipoles in the visible to the infrared region. In addition, the decay times of fluorophores were also reduced near the Ni substrates, suggesting both an enhanced electric field and a plasmon-coupling component are the mechanisms for fluorescence enhancement, similar to MEF substrates made from silver, copper, and gold nanoparticles. Our results show that nickel nanoparticles are suitable for enhancing near-infrared fluorescence, to a similar degree as Ag nanoparticles, and, therefore, are particularly applicable to the many whole blood biological assays in use today.

## Introduction

Near-infrared fluorescence is attractive in many settings, such as optical imaging and immunoassays, because it circumvents some of the typical problems associated with fluorescence in the visible region. Although visible dyes are bright, they, in turn, must compete with strong background fluorescence signals typical from biological samples. Autofluorescence is significantly diminished in the near-IR because few biological molecules (intrinsic chromophores) fluoresce in that spectral region.<sup>1,2</sup> However, the detection limits and sensitivity are still limited by the photostability and quantum yield of the near-IR fluorophore (label) and, therefore, still remain primary concerns in fluorescence spectroscopy and imaging today. In recent years, our laboratories have developed many applications of metal-enhanced fluorescence (MEF),<sup>3–7</sup> whereby metallic nanostructures favorably modify the spectral properties of fluorophores and alleviate some of their more classical photophysical constraints,<sup>3,6,7</sup> such as low quantum yield and poor photostability. Although the mechanism of metal-enhanced fluorescence is still being developed by Geddes and co-workers in a unified plasmon-fluorophore description,<sup>8</sup> our current explanation of plasmon–lumophore interactions is subtly different than our own early reports,<sup>3</sup> where it was postulated that it was the fluorophore itself that radiated, its photophysical properties thought to be modified by a resonance interaction with the close proximity to surface plasmons. Our laboratories' current mechanistic interpretation of MEF is underpinned by a model whereby nonradiative energy transfer occurs from excited distal fluorophores to surface plasmons in noncontinuous films (Figure 1, left), in essence, a fluorophore-induced mirror dipole in the metal. The surface plasmons, *in turn*, radiate the photophysical characteristics of the coupling fluorophores.

In essence, the *system radiates* as a whole. As a result, the *system* exhibits modified overall radiative rates, in contrast to the fluorophore itself. Ultimately, the increased radiative rate for the system lends to enhanced fluorescence signals (or increased system quantum yields) for fluorophores in close proximity to metallic structures, which we have shown can be represented by the following equations

$$Q_m = (\Gamma + \Gamma_m)/(\Gamma + \Gamma_m + k_{nr}) \quad (1)$$

where  $\Gamma$  is the unmodified *system* radiative decay rate,  $\Gamma_m$  is the metal-modified system radiative decay rate, and  $k_{nr}$  is the nonradiative decay rate, which is thought, for the most part, to be unchanged. The metal-modified lifetime,  $\tau_m$ , of a fluorophore–metal system is also decreased by the increased system radiative decay rate according to the equation

$$\tau_m = 1/(\Gamma + \Gamma_m + k_{nr}) \quad (2)$$

It is interesting to note that these rate equations are extensions of classical far-field fluorescence expressions and are only *loosely* thought to approximate the fluorophore–metal-coupled system.

The selection of fluorophores for MEF-based applications is underpinned by the choice of metal because the extinction properties ( $C_E$ ) of the metal are thought to play an important role in MEF.<sup>9–12</sup> Interestingly, MEF is readily thought to be underpinned by two very fast metal–fluorophore interactions: (1) an enhanced absorption, the wavelength dependence of which can be modeled using numerical simulations, solutions to Maxwells equations, and (2) an excited-state fluorophore–metal plasmon coupling, the wavelength dependence and other properties being predicated from the scattering portion

\* Corresponding author. E-mail: geddes@umbi.umd.edu.

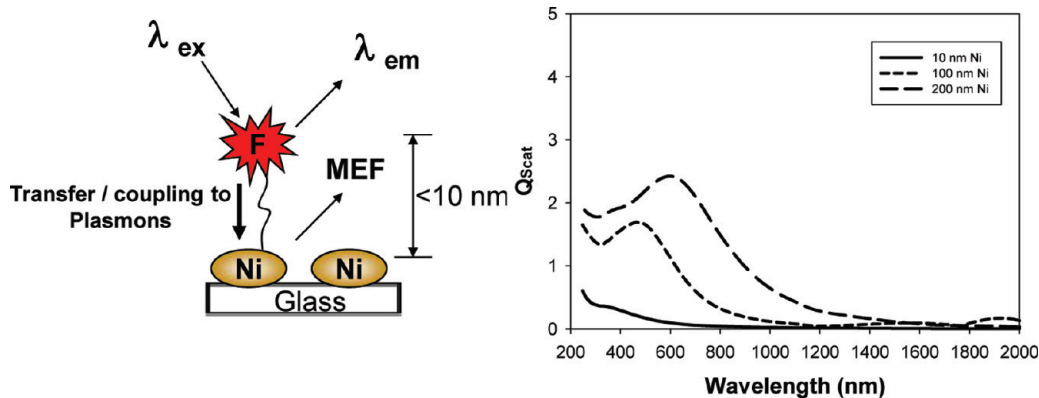


**Figure 1.** (Left) Schematic representation of metal-enhanced fluorescence. (Right) Calculated Mie scattering cross section for a 10, 100, and 200 nm Ni nanoparticle in water.

of the metal-particle extinction. The absorption ( $C_A$ ) and scattering ( $C_S$ ) portions of the extinction are given by

$$C_E = C_A + C_S = k_1 \text{Im}(\alpha) + (k_1/6\pi)|\alpha|^2 \quad (3)$$

where  $k_1 = 2\pi n_1/\lambda_0$  is the wave vector of the incident light in the surrounding medium (typically, air, water, or polymer film),  $\alpha$  is the polarizability of the sphere with radius  $r$ ,  $n_1$  is the refractive index of the medium, and  $\lambda_0$  is the incident wavelength. The term  $|\alpha|^2$  is the square of the modulus of  $\alpha$

$$\alpha = 4\pi r^3(\epsilon_m - \epsilon_1)/(\epsilon_m + 2\epsilon_1) \quad (4)$$

where  $\epsilon_1$  and  $\epsilon_m$  are the dielectric and the complex dielectric constants of the media and the metal, respectively. Given that particle plasmon resonances are size-dependent, Figure 1, right, shows the comparison of the scattering spectra of 10, 100, and 200 nm nickel nanoparticles (spherical) in water, calculated using traditional Mie theory. The extinction spectrum is dominated by the scattering component from the vis to the NIR range. It is, therefore, expected that close-proximity fluorophores would demonstrate enhanced properties near nickel nanoparticles, where the fluorophore emission spectral overlap with the scattering portion of the nanoparticle extinction provides for the plasmon-coupling enhancement effect in MEF.

To date, MEF from plasmonic nanostructured materials, such as silver,<sup>13–16</sup> gold,<sup>17</sup> copper,<sup>11</sup> zinc,<sup>9</sup> and chromium,<sup>18</sup> has been observed by our lab. In this regard, silver, gold, and copper nanoparticles were used for applications of MEF with fluorophores emitting in the visible wavelength region, whereas zinc and chromium nanostructured films were shown to enhance the fluorescence emission of fluorophores in the UV and blue spectral regions, respectively. In this paper, we subsequently show that nickel nanoparticulate films can be used as substrates for potential near-IR MEF applications, with similar electric field intensities as silver from 500 to 700 nm, but more intense in the near-IR and IR regions.

Nickel nanodeposits of various thicknesses were deposited, using thermal vapor deposition, onto glass microscope slides, which were characterized by optical absorption and atomic force microscopy (AFM) techniques. Several fluorophores with emission wavelength maximums ranging from 420 to 810 nm and with different free-space quantum yields were deposited onto nickel substrates in a sandwich sample format. Enhancement of fluorescence emission from fluorophores was both compared

and observed. In addition, we have observed a shorter fluorescence lifetime (decay time) for fluorophores in close proximity to Ni nanostructures, which is in complete agreement with other reports and trends for metal-enhanced fluorescence from silver<sup>6–8</sup> and eq 2, which approximates the coupled-system lifetime, suggesting that both an enhanced electric field and a plasmon-coupling component underpin the mechanism for fluorescence enhancement, similar to substrates made from silver, copper, and gold nanoparticles.<sup>11–13</sup>

## Experimental Section

**Materials.** All fluorophores, including Perylene, IR792, fluorescein isothiocyanate (FITC), Acridine Orange, Rose Bengal, Rhodamine 101, and Nile Blue, were obtained from Sigma-Aldrich Chemical Company and used as received. Silane-prep glass microscope slides were purchased from Sigma-Aldrich. Nickel nanostructured films of various thicknesses were deposited onto silane-prep glass microscope slides using thermal vapor deposition (AccuCoat, Inc., Rochester, NY).

**Preparation of Sandwich Format Samples for Metal-Enhanced Fluorescence Measurements.** A solution of 200  $\mu\text{L}$  of a fluorophore (500  $\mu\text{M}$ ) was sandwiched between two glass slides for the control sample and between one glass and one nickel nanostructured film or between two nickel nanostructured films. Each dye was excited with a source of appropriate wavelength and the fluorescence emission spectra measured, as described below. The concentration of all dyes was a constant 500  $\mu\text{M}$ .

**Optical Spectroscopy.** The absorption spectra of the nickel nanostructured films of varying thicknesses were collected using a Varian Cary 50 UV–vis spectrophotometer. Fluorescence spectra of the fluorophores were measured with blank glass sandwiches and glass–nanostructured film sandwiches using an Ocean Optics HD2000 fluorometer.

**Time-Domain Lifetime Measurements.** Time-domain lifetime measurements of the fluorophores were measured in a cuvette (solution), glass slide sandwiches, and glass–nickel substrate sandwiches in a front-face geometry using a Horiba Jobin Yvon TemPro system with pulsed laser diodes and appropriate filters. The data were fitted to one and multiexponential decay kinetics using impulse reconvolution analysis with a  $\chi^2$  goodness-of-fit criterion.

**Atomic Force Microscopy (AFM).** AFM images were obtained on a molecular imaging PicoPlus microscope. Samples were imaged at a scan rate of 1 Hz with a  $512 \times 512$  pixel resolution in a tapping mode.

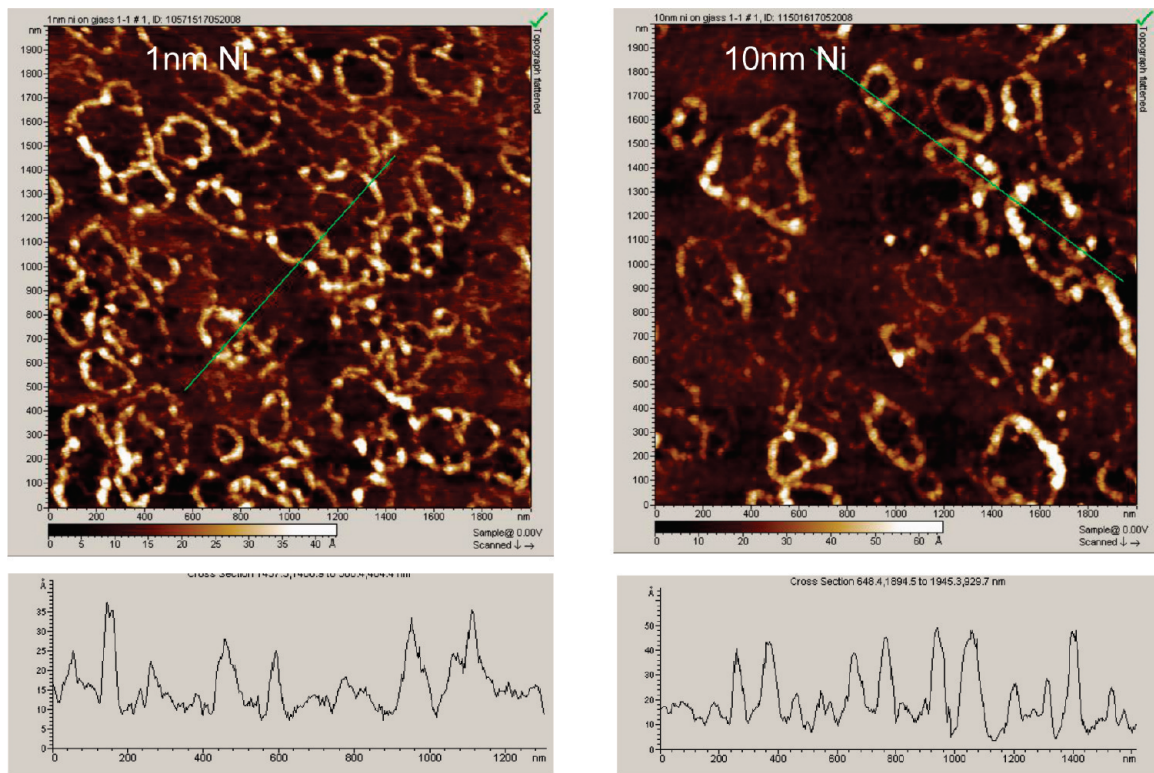


**Figure 2.** AFM images of (left) 1 nm Ni film on glass and (right) 10 nm Ni film on glass. Bottom scans are the respective line scans of AFM images for 1 nm Ni film on glass and 10 nm Ni film on glass.

**Mie Scattering.** Mie scattering calculations for 10, 100, and 200 nm diameter nickel nanoparticles in water were performed using freeware MieCalc software version 1.5.

**FDTD Calculations.** The FDTD method was employed here to determine the relative electric field intensities and distributions at the surface of nickel nanoparticles in a total field scattered field (TFSF), recalling that an enhanced e-field is one of the two mechanisms thought to contribute to fluorescence enhancement. TFSF sources are used to divide the computation area or volume into total field (incident plus scattered field) and scattered field only regions.<sup>19,20</sup> The incident *p*-polarized electric field is defined as a plane wave with a wave vector that is normal to the injection surface. The scattered and total fields were monitored during the simulation such that the total or scattered transmission can be measured. Using Lumerical FDTD Solution software, the simulation region is set to  $800 \times 800 \times 800$  nm with a mesh accuracy of 6. The overall simulation time was set to 500 ns and calculated over a frequency range from 300 to 800 nm for silver nanoparticles and from 300 to 800 nm for the nickel nanoparticles.

## Results and Discussion

The surface morphology of metal nanostructured films provides for different properties in metal-enhanced fluorescence.<sup>21</sup> Therefore, the morphology of different thicknesses of nickel films was studied using AFM. AFM images of 1 and 10 nm Ni films are shown in Figure 2, and other thicknesses of Ni films are provided in Figure 7 in the Supporting Information. From Figure 2, it can be seen that separated islands were formed when 1 and 10 nm Ni films were deposited on the glass slides. However, for the 1 nm Ni film, the height of the islands was below 2 nm, as seen from the line scan results. For the 10 nm Ni film (Figure 2, right), the height of the separated islands was below 3 nm, which was much lower than the thickness of

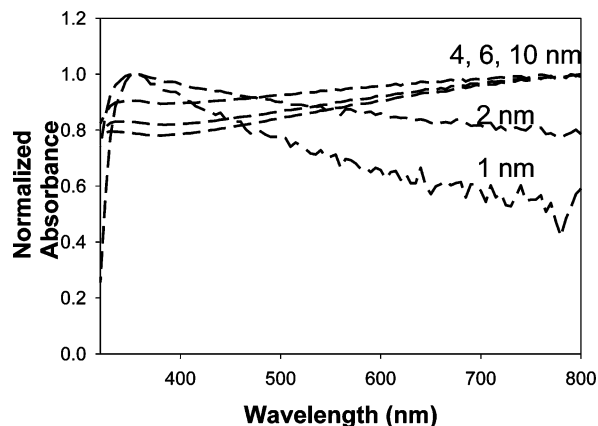


**Figure 3.** Normalized absorption spectra of vapor-deposited metallic Ni of various thicknesses deposited onto glass slides.

the Ni film measured by the quartz crystal microbalance (QCM) in the thermal evaporator. It can be concluded from the AFM images that, for 1 nm Ni samples, only one layer of separated Ni islands was formed on the glass slides due to the height of the islands being close to the Ni film thickness measured by the QCM. When the Ni film thickness is increased, separated Ni islands form a continuous film on the glass slide, with the top layer covered by aggregated nickel islands. To confirm this, we subsequently measured the optical absorbance of the Ni films. Figure 3 shows the normalized absorption spectra of 1, 2, 4, 6, and 10 nm thick nickel nanodeposits. Nickel nanodeposits of 1 and 2 nm show an absorbance peak around 380 nm, suggesting a particulate film. With increasing thickness, a broad absorption spectrum was observed, which is indicative of the aggregation of the nanodeposits on the surface forming a continuous film, as is observed for silver nanoparticle deposits. In Figure 1 in the Supporting Information, the absorbance spectra of the different thicknesses of the Ni deposits

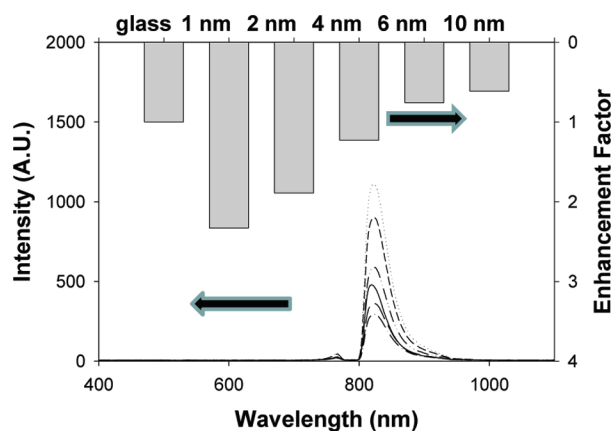


**Figure 4.** Emission spectra and fluorescence enhancement factors (top). Geometry schematic (bottom) for a solution of IR792 sandwiched between two Ni slides of varying thicknesses.

and the respective photographs show their transparency with decreased loading.

The fluorescence emission spectra of IR792 on different thickness Ni films and on glass are shown in Figure 4. Figure 4, bottom, shows the metal sandwich format. It can be seen that the fluorescence of IR792 is enhanced (2.5-fold) for 1 nm Ni as compared with the glass control sample, that is, no metal, with the enhancement factor decreased with increased Ni thickness. The fluorescence was diminished when the Ni thickness was greater than 6 nm, which, from both the AFM analysis and the absorption spectra, revealed that continuous films were formed. This finding is consistent with trends observed for continuous and particulate silver<sup>3</sup> and gold films<sup>12</sup> and their influence on MEF. We estimate the distance between the sandwich slides to be  $\approx 1 \mu\text{m}$ , and, in this geometry, only  $\approx 4\%$  of the solution is believed to be in the plasmon-enhancing range.<sup>3</sup> This suggests the near-field enhanced fluorescence is  $\approx 50$ -fold brighter.

The fluorescence emission spectra of Rhodamine 101 on different thickness Ni films and on glass are shown in Figure 5. For the different thicknesses of Ni on glass slides, as compared to bare glass slides, little enhanced fluorescence was observed. For Rhodamine 101, the emission peak is located at  $\approx 530 \text{ nm}$ ; however, for IR792, the emission peak is located at  $\approx 820 \text{ nm}$ , this finding suggesting both a wavelength and a quantum yield dependence of metal-enhanced fluorescence on the Ni films, similar to that observed for silver.<sup>22</sup>

In addition, several other fluorophores were studied on nickel substrates and are given in the Supporting Information, Figures S2–S6. We observed that the fluorescence intensity for Perylene, FITC, Acridine Orange, Rose Bengal, and Nile Blue is *apparently quenched* in a conventional metal–metal (Ni–Ni) sandwich format. Interestingly, for a metal–glass sandwich, that is, Ni–glass, the apparent quenching is not observed, with significant enhancements observed for some fluorophore/Ni combinations. As shown in Figure 1 in the Supporting Informa-

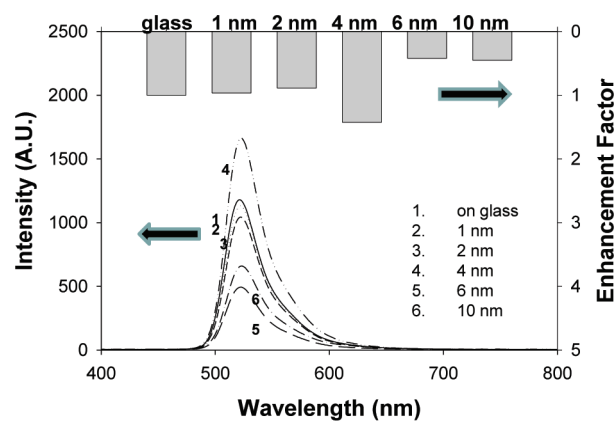


**Figure 5.** Emission spectra and fluorescence enhancement factors (top). Geometry schematic (bottom) for a Rhodamine 101 solution sandwiched between two Ni slides of varying thicknesses.

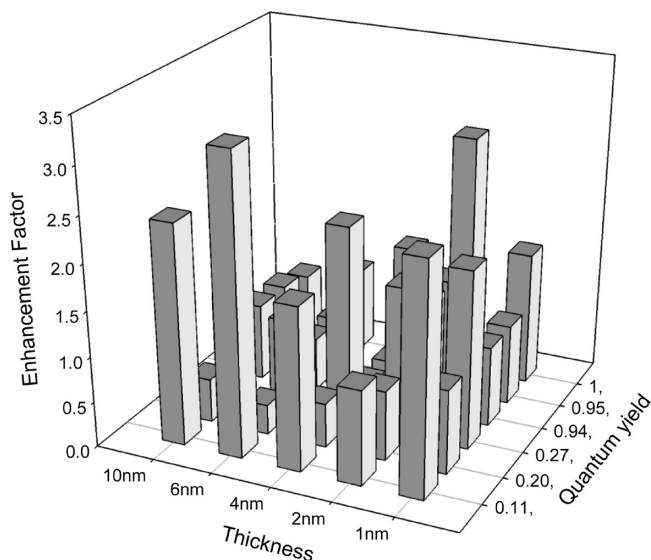


**Figure 6.** Metal-enhancement factor from fluorophores sandwiched between glass and Ni slides correlated with Ni film thickness and fluorophore free-space quantum yield,  $Q_0$ .

tion, right, thicker Ni films are no longer transparent or, indeed, particulate. It is, therefore, thought that metal–metal thick films may perturb the excitation intensity reaching the dye solution; therefore, for the rest of this work, metal–glass sandwiches are solely considered.

Figure 6 summarizes the enhancement factors observed for the fluorophores studied. Interestingly, fluorophores with the lowest free-space quantum yield generally appear to be enhanced the most, consistent with recent reports from our laboratory.<sup>23</sup>

In the Introduction, we suggested two complementary effects for the fluorescence enhancement: (i) surface plasmons can radiate coupled fluorescence efficiently, and (ii) an enhanced absorption or electric field facilitates enhanced emission. In this regard, we have simulated the wavelength dependence of the electromagnetic field around the Ni nanoparticles. When a luminophore is placed near metal, there is often a very strong

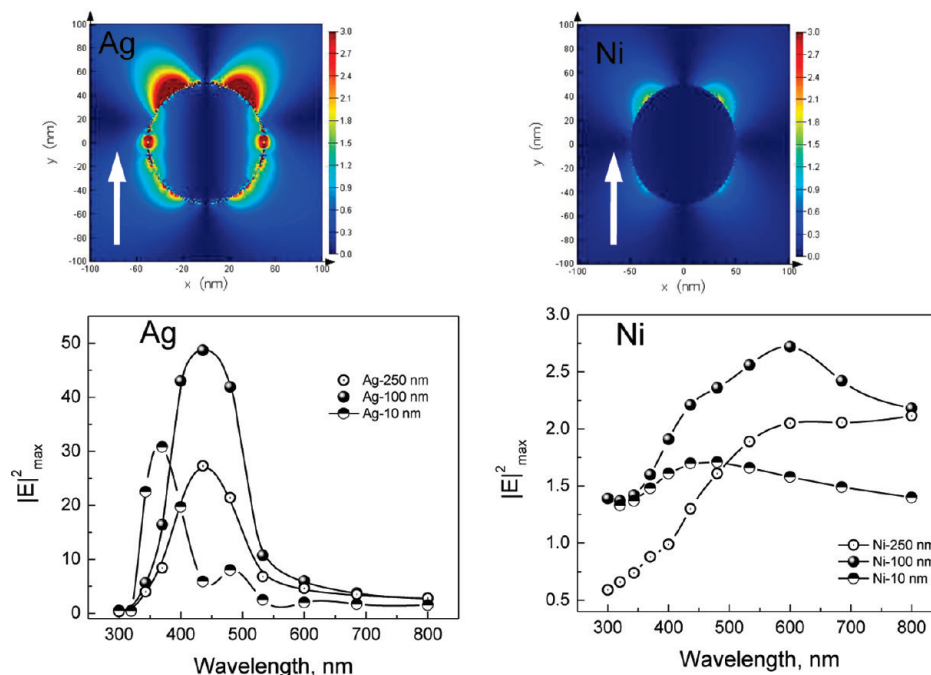
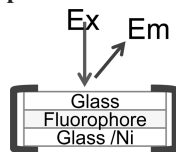


**Figure 7.** Dependence of electric field maximum intensity upon wavelength of the incident light (bottom). Calculations were undertaken using FDTD simulations for Ag and Ni nanoparticles of sizes 10, 100, and 250 nm (diameter). Top: typical images of near-field intensity distribution around 100 nm Ag and Ni nanoparticles. The white arrow shows the direction of the incident light injection. FDTD = finite-difference time-domain.

**TABLE 1: Tabulated Lifetime Values for FITC, Acridine Orange, IR792, and Nile Blue Measured from Glass and Ni Substrates Measured Using the Frequency-Domain and Time-Domain Technique. The Experimental Geometry Shows the Orientation of Samples and the Placement of the Fluorophore Solution with Respect to the Ni Surface**



	$\tau$ (ns)	A1 %	$\tau$ (ns)	A2 %	$\langle \tau \rangle$ (ns)	$\bar{\tau}$ (ns)	$\chi^2$
IR792 in cuvette	0.6	100			0.6	0.6	0.7
IR792 on glass/glass sandwich	0.1	36	0.6	64	0.4	0.5	0.8
IR792 on 2 nm Ni /glass	<0.1	100			<0.1		
Nile Blue in cuvette	0.8	100			0.8	0.8	0.9
Nile Blue on glass/glass sandwich	0.8	100			0.8	0.8	1.3
Nile Blue on 2 nm Ni/glass	0.4	13	0.8	87	0.7	0.7	1.4
FITC in H <sub>2</sub> O in cuvette	4.3	100			4.3	4.3	1.0
FITC on glass/glass sandwich	4.2	100			4.2	4.2	0.9
FITC on 1 nm Ni /glass	3.8	100			3.8	3.8	1.0
FITC on 6 nm Ni/glass	2.6	100			2.6	2.6	1.1
FITC on 10 nm Ni/glass	2.6	100			2.6	2.6	1.0

net absorption effect caused by the localized enhanced electromagnetic field of the incident excitation field. Because enhanced electromagnetic fields in proximity to metal nanoparticles are the basis for the increased system absorption in MEF, we have calculated the electric field enhancements (using FDTD calculations) for nickel nanostructures on a planar surface (Figure 7). We are aware that the morphology of the actual particles is not exactly the same, but we have chosen 10, 100, and 250 nm diameter particles to simplify and, indeed, approximate the calculation and, indeed, show the trends as a function of size. For Ni, FDTD calculations show that the maximum electric field intensity is predicted to occur over a broad range of wavelengths of  $\approx 300$  to 800 nm. In contrast, for silver, which is widely used in MEF,<sup>13,24</sup> the range of wavelengths is much narrower, from  $\approx 400$  to 500 nm, although similar intensities to silver occur in the 500–700 nm range. More importantly, the calculations

shown in Figure 7 predict that nickel nanoparticles can be used for MEF applications with fluorophores in a wide spectral range, with an intensity maximum in the near-IR, unlike the widely used silver,<sup>25,26</sup> which peaks in the visible. It should be noted that, although the electric field maximum for Ni peaks in the red, the plasmon scatter band is a maximum at much shorter wavelengths. This suggests that Ni nanoparticles will enhance fluorescence signatures over a broad wavelength range, not unlike what is shown in Figure 6, providing us with some confidence in our interpretation.

It has been suggested by Geddes and co-workers that the typically short lifetime observed for fluorophores near metallic nanoparticles is, indeed, indicative of the plasmon lifetime itself,<sup>27</sup> recalling that the coupled fluorophore quanta are radiated from the nanoparticles.<sup>27</sup> In this regard, the lifetime of FITC, IR792, and Nile Blue *near* nickel substrates was measured. The

experimental geometry and the overall results for the lifetime analysis are given in Table 1. The lifetime of IR792 on glass substrates (sandwich format, glass/IR792/glass) is similar to that for IR792 in a cuvette, as expected. Table 1 shows that the lifetimes of IR792 on glass and 2 nm Ni/glass are 0.4 ns and less than 0.1 ns, respectively. In addition, FITC and Nile Blue were measured and the respective data shown in Table 1. Subsequently, we observe that the lifetime of the fluorophore–metal system is reduced, as expected, due to a faster and more efficient fluorophore–plasmon emission, consistent with eq 2 and our laboratories' current interpretation of the MEF phenomenon.<sup>27</sup>

## Conclusions

We report the first observation of MEF from nickel substrates. Fluorophores with different emission wavelength maxima and free-space quantum yields in close proximity to nickel nanoparticles can undergo enhanced fluorescence; a 2.5-fold increase was observed from 1 nm Ni films from IR792 with up to a 10-fold enhancement observation from FITC. The wavelength dependence of the metal-enhanced fluorescence is not obvious as the maximum scattering bands and the e-field maximum occur at different wavelengths but can be correlated with numerical finite-difference time-domain simulations, showing a maximum for the enhanced electric field of Ni nanoparticles around 600 nm. In addition, the decay times of fluorophores were also reduced near the Ni substrates, suggesting that both an enhanced electric field and a plasmon-coupling component are the mechanisms for fluorescence enhancement, similar to substrates made from silver, copper, and gold nanoparticles. Our results subsequently show that nickel nanoparticles are suitable for enhancing near-infrared fluorescence, with potential application in whole unseparated blood immunoassays, where fluorophore emission intensity is a primary concern.

**Acknowledgment.** The authors acknowledge UMBI, the MBC, and the IoF for salary support.

**Supporting Information Available:** Absorption spectrum of vapor-deposited metallic Ni of various thicknesses; emission spectra, enhancement factors, and geometry schematics for Perylene, Acridine Orange, FITC, Rose Bengal, and Nile Blue solutions sandwiched between slides; and AFM images of Ni films on glass. This material is available free of charge via the Internet at <http://pubs.acs.org>.

## References and Notes

- (1) Cullum, M. E.; Lininger, L. A.; Schade, S. Z.; Cope, S. E.; Ragain, J. C., Jr.; Simonson, L. G. Diagnosis of militarily relevant diseases using oral fluid and saliva antibodies: Fluorescence polarization immunoassay. *Mil. Med.* **2003**, *168*, 915–921.
- (2) Davidson, R. S.; Hilchenbach, M. M. The use of fluorescent-probes in immunochemistry. *Photochem. Photobiol.* **1990**, *52*, 431–438.
- (3) Geddes, C. D.; Lakowicz, J. R. Metal-enhanced fluorescence. *J. Fluoresc.* **2002**, *12*, 121–129.
- (4) Aslan, K.; Lakowicz, J. R.; Szmajcinski, H.; Geddes, C. D. Metal-enhanced fluorescence solution-based sensing platform. *J. Fluoresc.* **2004**, *14*, 677–679.

- (5) Aslan, K.; Malyn, S. N.; Bector, G.; Geddes, C. D. Microwave-accelerated metal-enhanced fluorescence: An ultra-fast and sensitive DNA sensing platform. *Analyst* **2007**, *132*, 1122–1129.
- (6) Aslan, K.; Previte, M. J. R.; Zhang, Y. X.; Baillie, L.; Geddes, C. D. Ultra-fast and sensitive DNA hybridization assays: Application to genomic anthrax detection in <30 seconds. *Biophys. J.* **2007**, 552A.
- (7) Aslan, K.; Zhang, Y.; Hibbs, S.; Baillie, L.; Previte, M. J.; Geddes, C. D. Microwave-accelerated metal-enhanced fluorescence: Application to detection of genomic and exosporium anthrax DNA in <30 seconds. *Analyst* **2007**, *132*, 1130–1138.
- (8) Geddes, C. D. Metal-enhanced fluorescence II: Progress towards a unified plasmon-fluorophore description. *J. Fluoresc.* **2009**, in press.
- (9) Aslan, K.; Previte, M. J. R.; Zhang, Y.; Geddes, C. D. Metal-enhanced fluorescence from nanoparticulate zinc films. *J. Phys. Chem. C* **2008**, *112*, 18368–18375.
- (10) Pribik, R.; Aslan, K.; Zhang, Y.; Geddes, C. D. Metal-enhanced fluorescence from chromium nanodeposits. *J. Phys. Chem. C* **2008**, *112*, 17969–17973.
- (11) Zhang, Y.; Aslan, K.; Previte, M. J. R.; Geddes, C. D. Metal-enhanced fluorescence from copper substrates. *Appl. Phys. Lett.* **2007**, *90*, 173116.
- (12) Aslan, K.; Malyn, S. N.; Geddes, C. D. Metal-enhanced fluorescence from gold surfaces: Angular dependent emission. *J. Fluoresc.* **2007**, *17*, 7–13.
- (13) Aslan, K.; Lakowicz, J. R.; Geddes, C. D. Metal-enhanced fluorescence using anisotropic silver nanostructures: Critical progress to date. *Anal. Bioanal. Chem.* **2005**, *382*, 926–933.
- (14) Aslan, K.; Badugu, R.; Lakowicz, J. R.; Geddes, C. D. Metal-enhanced fluorescence from plastic substrates. *J. Fluoresc.* **2005**, *15*, 99–104.
- (15) Aslan, K.; Leonenko, Z.; Lakowicz, J. R.; Geddes, C. D. Fast and slow deposition of silver nanorods on planar surfaces: Application to metal-enhanced fluorescence. *J. Phys. Chem. B* **2005**, *109*, 3157–3162.
- (16) Aslan, K.; Lakowicz, J. R.; Geddes, C. D. Rapid deposition of triangular silver nanoplates on planar surfaces: Application to metal-enhanced fluorescence. *J. Phys. Chem. B* **2005**, *109*, 6247–6251.
- (17) Aslan, K.; Lakowicz, J. R.; Geddes, C. D. Nanogold-plasmon-resonance-based glucose sensing. *Anal. Biochem.* **2004**, *330*, 145–155.
- (18) Pribik, R.; Aslan, K.; Zhang, Y.; Geddes, C. D. Metal-enhanced fluorescence from chromium nanodeposits. *J. Phys. Chem. C* **2008**, *112*, 17969–17973.
- (19) Taflove, A.; Hagness, S. C. *Computational Electrodynamics: The Finite-Difference Time-Domain Method*, 2nd ed.; Artech House: Norwood, MA, 2000.
- (20) Anantha, V.; Taflove, A. Efficient modeling of infinite scatterers using a generalized total-field/scattered-field FDTD boundary partially embedded within PML. *IEEE Trans. Antennas Propag.* **2002**, *50*, 1337–1349.
- (21) Strelak, N.; Maskevich, A.; Maskevich, S.; Jardillier, J. C.; Nabeiv, I. Selective enhancement of Raman or fluorescence spectra of biomolecules using specifically annealed thick gold films. *Biopolymers* **2000**, *57*, 325–328.
- (22) Zhang, Y.; Dragan, A.; Geddes, C. D. Wavelength-dependence of metal-enhanced fluorescence. *J. Phys. Chem. C* **2009**, in press.
- (23) Zhang, Y.; Aslan, K.; Previte, M. J. R.; Geddes, C. D. Plasmonic engineering of singlet oxygen generation. *Proc. Natl. Acad. Sci. U.S.A.* **2008**, *105*, 1798–1802.
- (24) Aslan, K.; Leonenko, Z.; Lakowicz, J. R.; Geddes, C. D. Annealed silver-island films for applications in metal-enhanced fluorescence: Interpretation in terms of radiating plasmons. *J. Fluoresc.* **2005**, *15*, 643–654.
- (25) Aslan, K.; Gryczynski, I.; Malicka, J.; Lakowicz, J. R.; Geddes, C. D. *Metal-Enhanced Fluorescence: Application to High-Throughput Screening and Drug Discovery*; Wiley & Sons: Hoboken, NJ, 2005.
- (26) Aslan, K.; Gryczynski, I.; Malicka, J.; Matveeva, E.; Lakowicz, J. R.; Geddes, C. D. Metal-enhanced fluorescence: An emerging tool in biotechnology. *Curr. Opin. Biotechnol.* **2005**, *16*, 55–62.
- (27) Aslan, K.; Zhang, Y. X.; Geddes, C. D. Conversion of just-continuous metallic films to large particulate substrates for metal-enhanced fluorescence. *J. Appl. Phys.* **2008**, *103*, 084307.

JP900958N